PNAS RESEARCH ARTICLE | PHYSICS

Spin-resolved imaging of atomic-scale helimagnetism in mono- and bilayer NiI_2

Mao-Peng Miao[a,1], Nanshu Liu[b,c,d,1], Wen-Hao Zhang[a], Jian-Wang Zhou[a], Dao-Bo Wang[a], Cong Wang[b,c], Wei Ji[b,c,2], and Ying-Shuang Fu[a,e,2]

Affiliations are included on p. 7.

Edited by Risto Nieminen, Aalto-yliopisto Teknillisen fysiikan laitos, Espoo, Finland; received November 4, 2024; accepted August 10, 2025

Noncollinear magnetic orders in monolayer van der Waals magnets are crucial for probing delicate magnetic interactions under minimal spatial constraints and advancing miniaturized spintronic devices. Despite their significance, achieving atomic-scale identification remains challenging. In this study, we utilized spin-polarized scanning tunneling microscopy and density functional theory calculations to identify spin-spiral orders in mono- and bilayer NiI_2, grown on graphene-covered SiC(0001) substrates. We found two distinct spin-spiral states with $\boldsymbol{Q}$ vectors aligning and deviating by 7° from the lattice direction, exhibiting periodicities of 4.54 and 5.01 times the lattice constant, respectively. These findings contrast with bulk properties and align closely with our theoretical calculations. Surprisingly, the nonmultiples of spin spirals within finite-sized magnetic domains induce net magnetic moments, facilitating collective spin switching behavior under magnetic fields. Our research reveals intrinsic noncollinear magnetism at the monolayer limit with atomic-scale resolution, paving the way for exploring spin phenomena.

STM | van der Waals | magnetism

Significance

Intrinsic noncollinear magnetism deepens the understanding of magnetic interactions under reduced dimensions and advances miniaturized spintronic applications. Yet, it remains elusive experimentally because its existence demands intricate competing magnetic interactions and also the lack of suitable experimental probes. Here, we achieve atomic-scale spin imaging of spin-spiral order in mono- and bilayer NiI_2 van der Waals crystals, using spin-polarized scanning tunneling microscopy. Our experiments identify the period and canted spin-spiral plane of the spin spiral in mono- and bilayer NiI_2, which are both different from its bulk value, but agree well with our first-principles calculations. This opens up a platform for studying unusual noncollinear spin excitations in two-dimensional (2D) limit.

Investigating intrinsic magnetic order in two-dimensional (2D) systems provides insights into the fundamental understanding of magnetic interactions under reduced spatial constraints and also drives advances in building miniaturized spintronic devices. Noncollinear magnetic order exhibits rich spin textures (1–4). Its interaction with spin-polarized current is highly efficient, which is a desirable merit for spintronic applications. While collinear ferromagnetic and antiferromagnetic orders have been discovered in numerous 2D van der Waals (vdW) magnets, the noncollinear counterpart is rarely explored experimentally (2, 5–7). This is presumably because its existence demands intricate magnetic interactions, which arise either from the competing nearest and higher neighbor Heisenberg exchange that leads to spin frustration or from the involvement of antisymmetric Dzyaloshinskii–Moriya interaction (DMI) due to inversion symmetric breaking and spin–orbital coupling (8, 9). Previous studies of noncollinear magnetism, including bulk magnets (1, 3) and monolayer magnets strongly coupling to substrates (8), are essentially of the three-dimensional form. While recent progress observed noncollinear spin texture in few layer vdW magnets via moiré stacking (6), a direct observation of the intrinsic noncollinear magnetism has been lacking in the monolayer limit yet.

The probe of noncollinear magnetism is also challenging because most of the magnetic sensitive techniques such as neutron scattering (10) is not applicable to films. Optical probes of magnetic circular dichroism and second harmonic generation (SHG) have been used in characterizing noncollinear magnetism (5–7). But they rely on the comparison with theoretical modeling and cannot determine specific $\boldsymbol{Q}$ vectors that characterize the propagating direction and period of the noncollinear spins. Real-space magnetic probes of quantum magnetometry and magnetic force microscopy (11, 12) cannot reach sufficient resolution to resolve the atomic-scale spin textures. Spin-polarized scanning tunneling microscopy (SPSTM) can reach atomic-scale spin resolution based on its record for spin-dependent electron tunneling currents (13), rendering it an ideal probe to characterize various magnetic orders (14–16).

Helimagnetism is a typical noncollinear magnetic order (4), in which localized spins gradually rotate within the spin-spiral plane along the array of magnetic ions, causing the trajectory of the spin vectors to form a spiral. Our system of choice is monolayer NiI_2, because its bulk form supports helimagnetic order that may survive down to monolayer (10, 17, 18). However, the magnetic order of monolayer NiI_2 remains an open issue. Various magnetic configurations, ranging from ferromagnetism (FM) (19–21), antiferromagnetism (AFM) (22), antibiskyrmion (23) to different types of helimagnetism (24–28), have been predicted from first-principles calculations. Moreover, monolayer NiI_2 is

Author contributions: W.J. and Y.-S.F. designed research; M.-P.M. and N.L. performed research; W.-H.Z., J.-W.Z., D.-B.W., and C.W. contributed new reagents/analytic tools; M.-P.M., N.L., W.J., and Y.-S.F. analyzed data; and M.-P.M., N.L., W.J., and Y.-S.F. wrote the paper.

The authors declare no competing interest.

This article is a PNAS Direct Submission.

[1]M.-P.M. and N.L. contributed equally to this work.

[2]To whom correspondence may be addressed. Email: wji@ruc.edu.cn or yfu@hust.edu.cn.

This article contains supporting information online at https://www.pnas.org/lookup/suppl/doi:10.1073/pnas.2422868122/-/DCSupplemental.

Published September 23, 2025.

expected to be a type-II multiferroic candidate. While recent SHG studies suggest the existence of multiferroic states in monolayer NiI_2 (29), interpretations of the experimental results are under debate (7, 30, 31). Those studies render the precise determination of its spin state crucial to resolve the controversy.

Here, using SPSTM, we achieved spin-resolved imaging of helimagnetism at atomic scale in both mono- and bilayer NiI_2. Spin-spiral states are identified to propagate along (7° off) the lattice direction with a periodicity of 4.54 (5.01) times the lattice constant for the monolayer (bilayer) NiI_2. Such propagation vectors are different from the bulk value or its in-plane projection, but agree well with our first-principles calculations. The monolayer spin spiral surprisingly indicates collective spin switching behavior under magnetic field, as originated from net magnetic moments due to the nonmultiples of spin spirals inside a finite-sized domain. Our study opens up an avenue for studying the unusual spin excitations with noncollinear spins.

The experiments were performed with a custom-made Unisoku STM (1500) system at 2 K (15). High-quality mono- and bilayer NiI_2 films were grown with molecular beam epitaxy on graphene-covered SiC(0001) substrate. Detailed descriptions of the experiments and the density functional theory (DFT) calculations are depicted in *Materials and Methods*.

Results

Bulk NiI_2 is a vdW crystal that belongs to trigonal $\bar{R}3m$ space group ($CdCl_2$ prototype) at room temperature. Its each vdW layer consists of a triangular lattice of Ni layer sandwiched between two I layers, with each Ni cation ($3d^8$, S = 1) octahedrally coordinated by six I anions, forming a 1-T structure (Fig. 1*A*). The vectors $\boldsymbol{a}$ and $\boldsymbol{b}$ in Fig. 1*A* serve as the lattice vectors for the unit cell of the NiI_2. With decreasing the temperature, bulk NiI_2 undergoes two successive magnetic phase transitions to an interlayer AFM state at 75 K and a proper-screw helimagnetic state with a $\boldsymbol{Q}_{bulk}$ vector of (0.1384, 0, 1.457) at 59.5 K (10, 17, 18). While the helimagnetic state in bulk NiI_2 has been well established, its monolayer form remains an open issue.

The as-grown NiI_2 films were first characterized using a conventional spin-averaged W tip. Its topographic image displays atomically flat surfaces (Fig. 1*B*). The apparent height of the monolayer (bilayer) film is measured as 8.50 Å (7.30 Å) at a sample bias of +1.0 V (*SI Appendix*, Fig. S1), conforming to its expected monolayer height. An atomic-resolution STM image of the monolayer NiI_2 film shows its in-plane lattice constant of the top-layer I (a_0) is 3.88 Å (Fig. 1*C*), which is consistent with the previously reported theoretical values ranging from 3.88 to 3.98 Å (20–22, 32).

High-bias STM images of the NiI_2 monolayer usually contain a considerable density of dark spots (Fig. 1*D*), which vanish upon imaging at low sample biases (*SI Appendix*, Fig. S2), revealing intact atomic lattice of top layer I. Those spots can be controllably created, erased, and moved with the STM tip (*SI Appendix*, *Supplementary Note 1*), suggesting they are polarons (33) rather than atomic defects, as reported by us in $CoCl_2$ and $FeCl_2$ films (34). Typical tunneling spectra (Fig. 1*E*) acquired at the polaron-free region of the monolayer (bilayer) surface feature a large insulating gap of 2.03 eV (1.76 eV), where the conduction band minimum and valence band maximum are located at +0.25 (+0.04) and −1.78 eV (−1.72 eV), respectively. The insulating gaps are off-centered due to the different work functions of graphene (4.62 eV) and NiI_2 (5.62 eV) (35, 36).

We investigate its magnetic state using SPSTM with an Fe-coated tip, which possesses in-plane spin sensitivity and can be aligned along magnetic fields (13, 37). As shown in Fig. 1*D*,

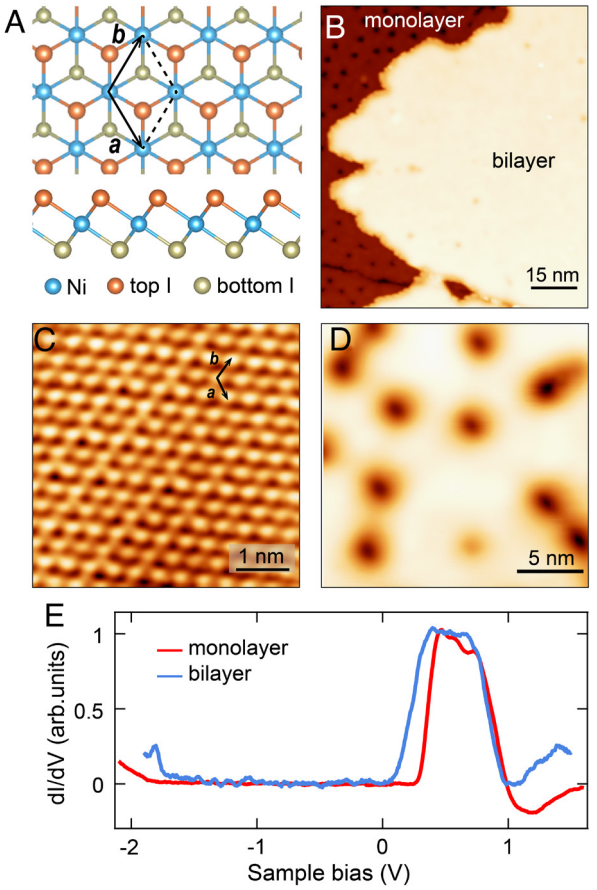

Fig. 1. Morphology and electronic structure of mono- and bilayer NiI_2 measured with a conventional spin-averaged W tip. (*A*) *Top* view (*Up*) and *side* view (*Down*) of the crystal structure of monolayer NiI_2. (*B*) Large-scale STM topographic image of NiI_2 film (V_s = +1.0 V, I_t = 5 pA). (*C*) Atomic resolution of the STM image (V_s = +0.1 V, I_t = 20 pA) of monolayer NiI_2. (*D*) Spin-averaged STM image (V_s = +0.65 V, I_t = 10 pA) of monolayer NiI_2. (*E*) Tunneling spectra (V_s = +1.6 V, I_t = 100 pA, V_{mod} = 30 mV) measured on mono- and bilayer NiI_2 film. The conduction band has a negative differential conductance in the monolayer spectrum, reflecting its flat dispersion.

the polarons exhibit a prominent contrast in the image, which obscures the spin-contrast. To avoid it, we "cleaned out" all apparent polarons from a selected region of interest via STM manipulation. Fig. 2*A* shows an SPSTM image of such a cleaned surface region at the same bias setting of 0.65 V as the non-spin-polarized measurements (Fig. 1*D*). Distinct to Fig. 1*D*, the SPSTM image displays clear stripe patterns without external magnetic field. Upon application of an out-of-plane −1 T field, the stripe pattern shifts drastically relative to a defect marker (Fig. 2 *A* and *B*, red circles). The marker is from a real crystal defect and cannot be manipulated. Such stripe patterns are not observable with conventional nonmagnetic W tips. This convincingly indicates the stripe pattern is a spin contrast. Measuring the stripe pattern of adjacent domains with an identical Fe tip further substantiates the pattern is due to a spin-polarization of the sample, instead of an electronic effect (*SI Appendix*, *Supplementary Note 2*).

Such stripe pattern could be from either an AFM state or a spin spiral. To distinguish them (16), we have systematically investigated the response of the stripe pattern to different magnetic fields (*SI Appendix*, Figs. S5 and S6). The stripe pattern progressively shifts relative to the defect marker with increasing field and saturates at +0.5 T (Fig. 2*C* and *SI Appendix*, Fig. S7), a typical field for fully aligning the Fe tip magnetization to out-of-plane (13, 37). The shifting directions and saturation fields are opposite for

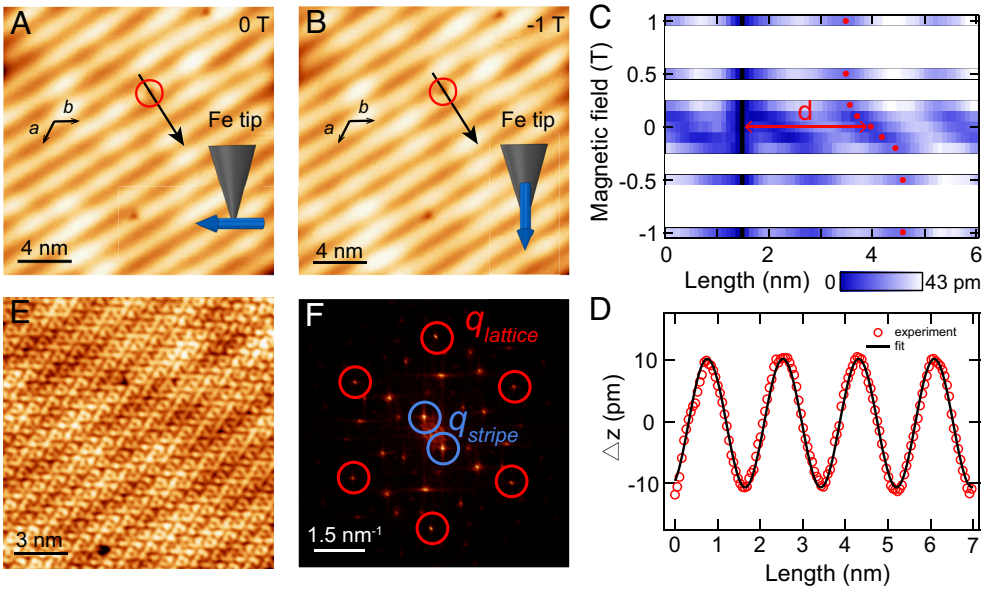

Fig. 2. Spin mapping of the spin-spiral texture in monolayer NiI_2 with the ferromagnetic Fe tip. (*A* and *B*) SPSTM images (V_s = +0.65 V, I_t = 10 pA) of monolayer NiI_2 under different magnetic fields. An I vacancy defect is marked with red circles. The Fe-tip magnetization is depicted with blue arrows. The black arrows mark the unit vectors of the I lattice. (*C*) 2D plot of line profiles taken across the defect marker (black lines in *A* and *B*) under different magnetic fields. Red dots mark locations of a selective dark stripe, whose distance, *d*, relative to the marker is marked with a red arrow segment. (*D*) The red dotted line is extracted across the stripe pattern. The solid black lines are the fittings to the data with the sine function. (*E*) High-resolution of the SPSTM image (V_s = +0.2 V, I_t = 10 pA) of monolayer NiI_2, showing coexistence of the atomic lattice and stripe pattern. (*F*) FFT image of (*E*). The diffraction spots for the lattice $q_{lattice}$ and the spin stripe q_{stripe} are marked.

different field polarities. This demonstrates the stripe pattern is from a spin spiral, instead of an AFM state, since the AFM spin contrast does not shift continuously with respect to gradually canted tip-magnetization. Moreover, line profile across the stripe pattern displays a sine-wave shape (Fig. 2*D*), conforming to the expectations of a spin-spiral state (16). We have evaluated the possible influence of Landau levels from the bilayer graphene substrate on the spin stripes. No clear Landau levels were observed at 4 K up to 8 T (*SI Appendix*, Fig. S8), probably because the bilayer graphene/SiC interface causes potential fluctuations, smearing out the Landau levels.

The spatial period of the stripes is measured as 17.6 Å, corresponding to $4.54a_0$. As shown in Fig. 2 *E* and *F*, the spin-spiral propagation, defined as being perpendicular to the stripes, lies along the lattice direction in real space (*SI Appendix*, Fig. S9). Given both the periodicity and the orientation of the spin spiral, its propagation vector $\boldsymbol{Q}_{1L}$ in reciprocal space is thus inferred as (0.110, 0.110, 0) (See *Materials and Methods* and *SI Appendix*, Fig. S10 for the definition of $\boldsymbol{Q}$).

Since the finite stray field of the Fe-coated tip may potentially perturb the monolayer spin spiral, we performed measurements using an AFM Cr-coated tip with a negligible stray field, whose magnetization is invariant against magnetic field. Fig. 3 *A*–*D* show a series of SPSTM images taken with the Cr tip on monolayer NiI_2 of ~2,000 nm^2 under different magnetic fields, showing clearly resolved stripe patterns relative to a defect marker. The spin contrast is also reflected in spin-polarized spectra (Fig. 3*E*) acquired at bright and dark stripes, revealing spin asymmetry as a function of energy. The stripe pattern is robust against low magnetic fields, but abruptly reverses its contrast upon the field exceeding ~±2 T (Fig. 3 *A*–*D* and *SI Appendix*, Fig. S11), resulting in a hysteresis loop of the contrast (Fig. 3*F*). As the tip magnetization is unchanged, such switching originates from the spin-spiral state, as further confirmed with Fe-coated W tips (*SI Appendix*, *Supplementary Note 3*). It is worth to mention that the spin-spiral domains can be switched to other equivalent directions during scanning (*SI Appendix*, *Supplementary Note 4*), indicating the energy barrier is small.

Previous studies on spin-spiral states suggest the local magnetizations are titled toward the field direction, resulting in change of the $\boldsymbol{Q}$ vector rather than spin switching (39–41). The switching behavior demonstrates our spin spiral has residual magnetic moment and its neighboring spin moments are strongly coupled. We conjecture that residual moment is rooted from the nonmultiples of spin spirals inside a finite size domain, causing imbalanced spin-up and spin-down components (*SI Appendix*, *Supplementary Note 5*). To examine such scenario, we measured the threshold switching field B_c at spin-spiral domains with different area *S* (Fig. 3*G*). Indeed, the spin-spiral remains unchanged up to our maximum field of 8 T upon *S* exceeding 10,000 nm^2, confirming to the calculated large energy difference (5.77 meV/Ni) between the spin-spiral ground state and ferromagnetic order (26). Below 10,000 nm^2, B_c increases approximately linearly with *S*, except when it is small (~1,000 nm^2) (Fig. 3*H*). This observation can be understood from the fact that B_c is inversely proportional to the net magnetic moment per unit area *M*/*S*, and the assumption that the net moment *M* is constant for all domains of different sizes. Such an assumption is based on the irregular domain boundaries with domain sizes way larger than the spin-spiral period and would be an interesting subject for mathematic study. When the domain sizes are small, the assumption breaks down, due to profound fluctuations in shapes of domain boundaries.

Having studied the monolayer films, we further identify the spin texture of the bilayer NiI_2. Its SPSTM images also resolve a stripe pattern corresponding to the spin-spiral state (Fig. 4*A* and *SI Appendix*, Fig. S16). However, its spiral period ($5.01a_0$) is larger than that of the monolayer ($4.54a_0$). Furthermore, the spin-spiral propagation direction is no longer along the lattice direction in real space, but propagates along a +7° direction off the lattice direction (Fig. 4 *A* and *B*). The intersecting angle of the spin-spiral propagation direction can also be −7° relative to the lattice direction, as is also observed in a different spin-spiral domain in Fig. 4 *C* and *D*.

To substantiate the experimental findings, we carried out first-principles calculations. A supercell characterized by vectors $\boldsymbol{m}_{1L}$ = (6$\boldsymbol{a}$, 3$\boldsymbol{b}$) and $\boldsymbol{n}_{1L}$ = (−3$\boldsymbol{a}$, 3$\boldsymbol{b}$) was utilized to model the

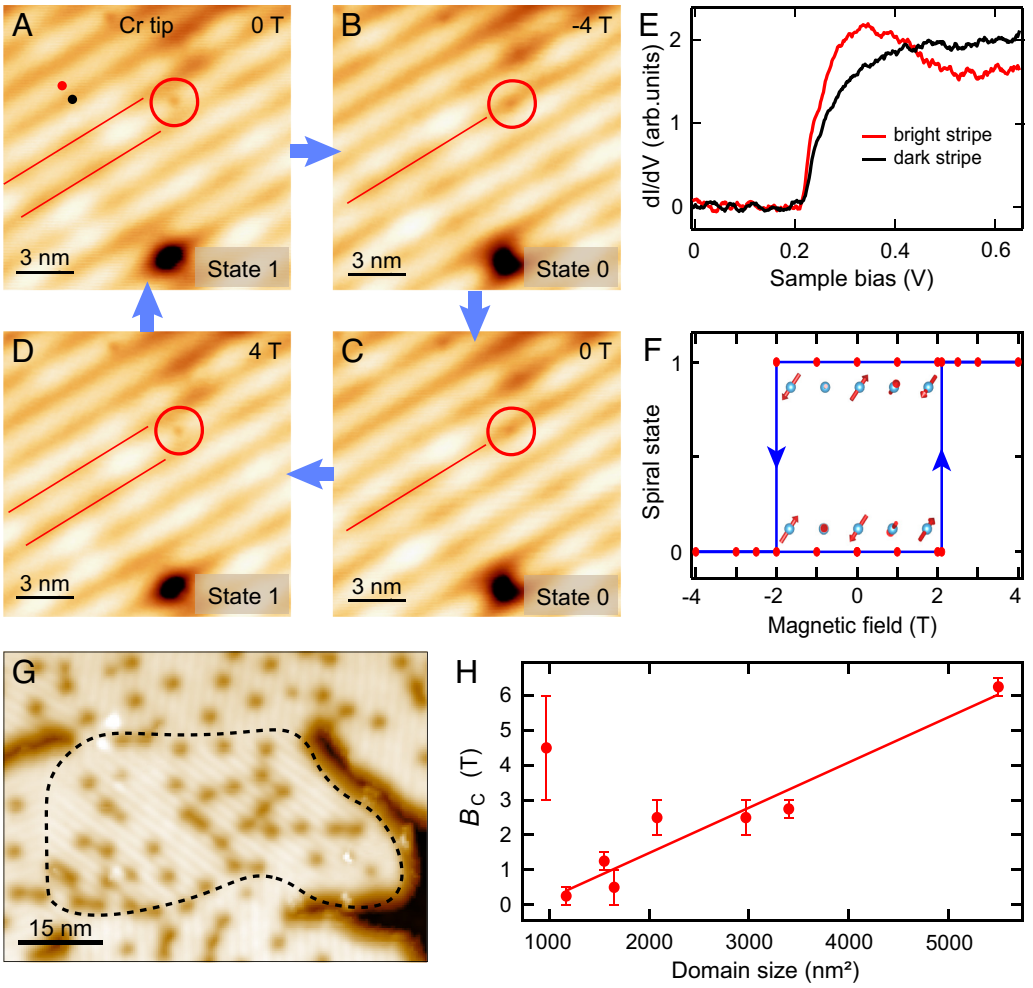

Fig. 3. Bistability of the spin-spiral state in monolayer NiI_2. (*A–D*) SPSTM images (V_s = +0.65 V, I_t = 10 pA) of monolayer NiI_2 taken with a Cr tip under different magnetic fields. An I vacancy is marked with red circles as a marker. The spin-spiral state is defined as "state 1" ("state 0") for the case of the defect marker residing on the bright (dark) stripes. The red lines selectively mark representative dark stripes. (*E*) Spin-polarized tunneling spectra (V_s = +0.65 V, I_t = 100 pA, V_{mod} = 5 mV) measured on the bright (red) and the dark stripe (black) of the monolayer NiI_2 film, whose spectroscopic locations are marked in (*A*). (*F*) Statistics of the spin-spiral state under different magnetic fields. The opposite local moments between the spin spiral "state 1" and "state 0" are depicted in the *Inset*. (*G*) Large-scale SPSTM image of a NiI_2 film (V_s = +0.65 V, I_t = 10 pA). Black dashed lines mark a typical spin-spiral domain. (*H*) Threshold flipping field B_c as a function of the domain area S measured with multiple Fe tips. The solid lines are the fittings to the data with the relation $B_c \propto S$. The fitting gives an intercept value of −1.1 ± 0.5 T, which might be due to the finite stray field of the ferromagnetic tip (38).

experimentally observed spin-spiral order (see the dashed diamond in Fig. 5*A* for more details). Given all the considered magnetic configurations, the one illustrated in this supercell shows the lowest energy. The order exhibits spin-spiral stripes (corresponding to stripes in SPSTM images) perpendicular to the lattice direction and presents a periodicity of $4.50a_0$ (gray shadowed rectangles in Fig. 5*A*) for the real-space propagating along the lattice direction, i.e., the x direction (equivalent to a spin-spiral propagation vector $\boldsymbol{Q}_{1L}$ = (1/9, 1/9, 0), i.e., (0.111, 0.111, 0) in reciprocal space). These features align with the experimentally inferred $\boldsymbol{Q}_{1L}$ = (0.110, 0.110, 0), corresponding to the propagating periodicity of $4.54a_0$ along x direction. It was noteworthy that the calculated spiral order is closely comparable to the most favorable magnetic order featuring a propagating vector of $\boldsymbol{Q}$ = (0.125, 0.125, 0) for the reciprocal space and a real-space periodicity of $4.00a_0$ in our previous DFT calculations (26). The magnetic easy axis is tilted to the NiI_2 layer plane, aligning with the Ni-I bond direction. The magneto-crystalline anisotropy A_z is predicted to be 1.43 meV (26), defined as the energy cost to rotate the magnetic moment from the z to the x direction. Despite a reduction in the absolute value of the Kitaev interaction in the monolayer relative to few-layer or bulk NiI_2, its strength remains considerably substantial compared to the single-ion magnetic anisotropy and the noncollinear spin–spin interaction (26). Therefore, this dominant Kitaev interaction sustains the rotational propagation of magnetic moments parallel to the Ni-I plane in monolayer NiI_2. The normal vector of spin-spiral plane and its in-plane projection form a polar angle θ relative to the z axis of 52° and an azimuth angle φ to the x direction of 30° (*SI Appendix*, Fig. S17) and nearly directs to the Ni-I bond (green arrow in Fig. 5*B*). This result is consistent with our previous publication (26) and ref. 27, but much different from those reported in ref. 28 with θ = 64°, φ = 0°. This conforms to our SPSTM measurements shown in *SI Appendix*, Fig. S18, which also suggest that the spiral plane may be canted (*SI Appendix*, *Supplementary Note 6*). Nevertheless, the precise polar angle θ and azimuth angle φ cannot be precisely determined experimentally, since the tilting angle of the tip magnetization is unknown.

Fig. 5*C* illustrates the spin density distribution associated with the x component of magnetic moments of Ni atoms in the spin-spiral order depicted in Fig. 5*A*, which displays alternating spin density stripes along the x direction. The stripe pattern exhibits a width of 17.7 Å, close to the experimentally measured value of 17.6 Å. The helimagnetism existed in a triangular lattice can

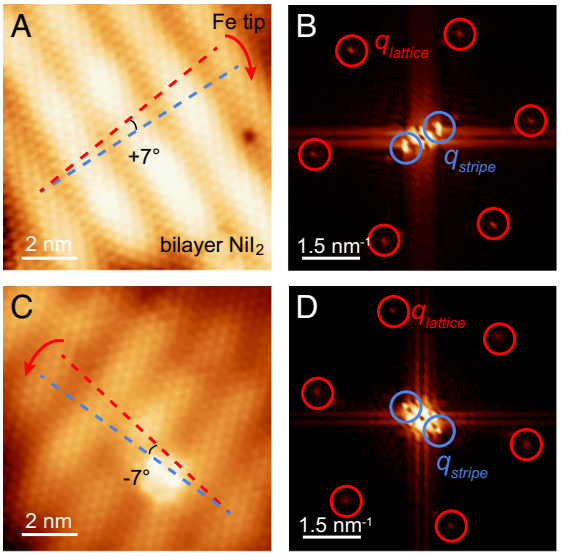

Fig. 4. Spin mapping of the spin-spiral texture in bilayer NiI_2 with the Fe tip. (*A*) High-resolution of the SPSTM image (V_s = +0.2 V, I_t = 100 pA) of bilayer NiI_2, showing coexistence of the atomic lattice and the spin-spiral stripe pattern. Red and blue dashed lines represent the direction of lattice and spin-spiral propagation, respectively. (*B*) FFT image of (*A*). The diffraction spots for the lattice vector $q_{lattice}$ and the spin stripe q_{stripe} are marked by red and blue circles, respectively. (*C*) Another spin-spiral domain with a different intersecting angle between the spin-spiral propagation direction and the lattice direction. (*D*) FFT image of (*C*).

be described using a frustrating J_1-J_3 model (42), which is extensively discussed in the literature (23–27), rather than by the Kitaev interaction. In monolayer NiI_2, the interplay between FM J_1 and AFM J_3 yields a $|J_1/J_3|$ value of 1.26 (26), which adequately conforms to the criterion, namely $|J_1/J_3| < 4$, for the emergence of noncollinear spin-spiral orders (42). Here, J_1, J_2, and J_3 denote the nearest, second nearest, and third nearest neighbor intralayer isotropic exchange parameters, which are indicated in Fig. 5*A* with arrows colored black, green, and purple, respectively.

For the NiI_2 bilayer, the spin-spiral feature persists with minor alterations in the orientation and period of the spin-spiral propagation compared to the monolayer. Fig. 5*D* shows the real-space distribution of the magnetic moments, where a supercell defined by vectors $\boldsymbol{m}_{2L}$ = (9$\boldsymbol{a}$, 11$\boldsymbol{b}$) and $\boldsymbol{n}_{2L}$ = (−2$\boldsymbol{a}$, 1$\boldsymbol{b}$) characterizes the bilayer order. This supercell encompassed two iterations of the bilayer spin-spiral order, featuring a spin-spiral propagation in an increased real-space period of 5.07a_0 and oriented 9.8° from the *x* direction (gray shadowed rectangles in Fig. 5*D*), reproducing the experimentally observed value of 5.01a_0 and approximately 7°. A larger supercell of (14$\boldsymbol{a}$, 16$\boldsymbol{b}$) and (−2$\boldsymbol{a}$, 1$\boldsymbol{b}$) (*SI Appendix*, Fig. S20) gives an angle to the *x* direction of 7.05° and period of 5.03a_0, closer to the experiment. Our calculations indicate that this supercell contains three iterations of spiral order and is indeed energetically undistinguishable to that in Fig. 5*D*. The two spin-spiral orders are, at least, 0.20 meV/Ni more energetically stable than other orders considered in this work (Fig. 5*E*). As spin-spiral orders were modeled using different integer-sized supercell periods, the simulated results are inevitably deviated from the experiment. Even so, we captured the magnetic ground states of monolayer and bilayer NiI_2 within an acceptable accuracy range. This marginal increase in the propagation period of bilayer is, most likely, ascribed to a significantly large interlayer second nearest neighbor exchange ($J_2^{\perp}$) and a $|J_2/J_1|$ ratio of 0.05 in the bilayer, which is reduced

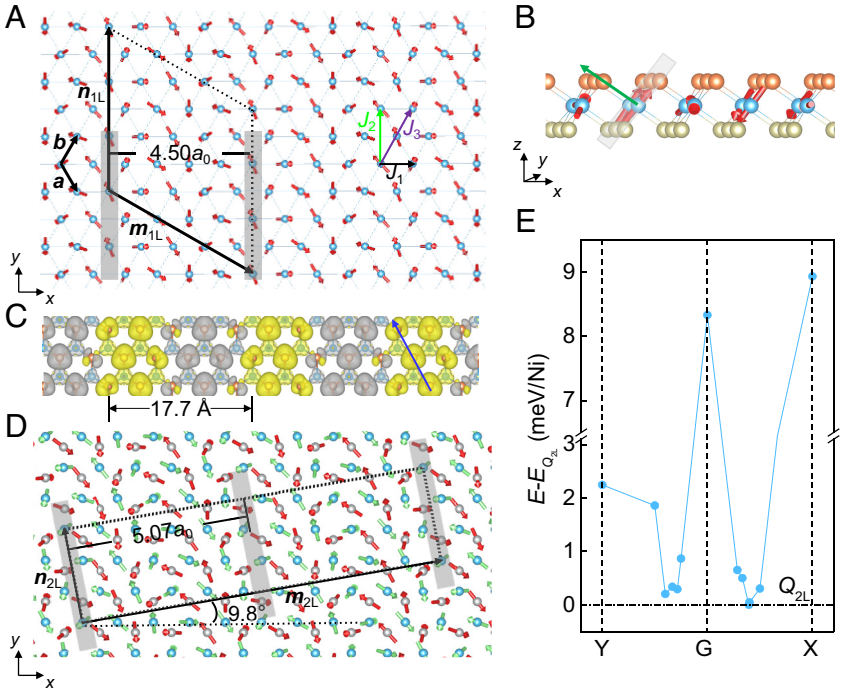

Fig. 5. Spin-spiral configurations of mono- and bilayer NiI_2 obtained from DFT calculations. (*A* and *B*) *Top* and perspective views of spin-spiral order for monolayer NiI_2, respectively. The geometrical structure in (*B*) is viewed along the blue arrow in (*C*). The spin-spiral plane is represented by a gray parallelogram. The green arrow in (*B*) depicts the normal vector of the Ni-I plane. The supercell of the spin spiral in (*A*) is indicated by a dashed black diamond with the two vectors of $\boldsymbol{m}_{1L}$ = (6$\boldsymbol{a}$, 3$\boldsymbol{b}$) and $\boldsymbol{n}_{1L}$ = (−3$\boldsymbol{a}$, 3$\boldsymbol{b}$), where $\boldsymbol{a}$ and $\boldsymbol{b}$ are the lattice vectors for the unit cell of monolayer NiI_2. The gray shadowed rectangles in (*A* and *D*) correspond to the "stripe pattern" of the magnetic order in the SPSTM experiment. (*C*) Spin density distribution associated with the *x* component of magnetic moments of Ni atoms with an isosurface value of 5 × 10^{-4} *e*/Bohr^3. Note that the bottom-layer I atoms and their spin densities are omitted for clarity. (*D*) *Top* view of spin-spiral order for bilayer NiI_2. The supercell in (*D*) is labeled by a dashed black parallelogram with the two vectors of $\boldsymbol{m}_{2L}$ = (9$\boldsymbol{a}$, 11$\boldsymbol{b}$) and $\boldsymbol{n}_{2L}$ = (−2$\boldsymbol{a}$, 1$\boldsymbol{b}$). The green and red arrows denote magnetic moments of Ni atoms in the upper and lower layers, respectively. The spiral periodicities are also labeled. (*E*) Comparison of total energies among various spiral orders in different supercells for bilayer NiI_2. The lowest energy of $\boldsymbol{Q}_{2L}$ is set to zero and indicated by a horizontal black dashed line.

compared to that in the monolayer (0.06) (26, 43). This is verified by the comparison of different interlayer distances, and the enlarged $J_2^{\perp}$ and reduced $|J_2/J_1|$ values in the bilayer NiI_2 with smaller interlayer distance (*SI Appendix*, Fig. S21 and Table S1). The NiI_2 layers are antiferromagnetically coupled due to the significantly large $J_2^{\perp}$. All magnetic moments in the bilayer order similarly rotate within the Ni-I plane, a manifestation of the significant Kitaev interaction (26). Here, the experimental unveiling of the spin-spiral order in the bilayer conclusively closes the uncertainty issue raised by the previous theoretical prediction (26) on the magnetic ground state for the bilayer. This finding further highlights that the coincidence points between the models of the spin-spiral and the monolayer may appear after every two or more spin-spiral stripes; for instance, vector $\boldsymbol{m}_{2L} = (9\boldsymbol{a}, 11\boldsymbol{b})$, defined by these coincidence points, across two spin-spiral stripes for the NiI_2 bilayer.

We further considered the impact of interface on the spin spirals. The vdW interactions dominate the NiI_2 and graphene interface and their interfacial interactions are much weaker than that between monolayer films of 3d transition metals and open 5d metal surfaces. Our DFT calculations on the freestanding monolayer and bilayer NiI_2 give spin spirals that match with our experiment well, demonstrating this model is a good approximation to the experiments, and the graphene substrate has no significant impact on the spin spirals. Moreover, in experiments, we found monolayer NiI_2 films can form different moiré patterns with the graphene substrate (*SI Appendix*, Fig. S22 *A* and *C*). Nevertheless, their measured spin spirals are identical (*SI Appendix*, Fig. S22 *B* and *D*), further substantiating the negligible impact of the substrate. Although epitaxial or other types of strain were able to change the magnetism of monolayer NiI_2 (26), we believe that the graphene substrate is insufficient to change the magnetic order of monolayer NiI_2. Therefore, NiI_2, most likely, retains its intrinsic properties on the graphene substrate.

Summary

In summary, we have identified distinct spin-spiral states with canted plane in mono- and bilayer NiI_2. The $\boldsymbol{Q}$ vectors vary with the layer thickness, which are different from the bulk value or its in-plane projection, but agree nicely with our DFT calculations. Our work clarifies the controversies over the magnetic configuration of monolayer NiI_2, which is crucial for understanding its anticipated type-II multiferroic state (7, 29–31, 44). Based on existing theories about spin-spiral induced ferroelectricity, we have further attempted to measure the possible ferroelectricity, which may induce local band bending adjacent to the film edges (45, 46). However, no signature of electric polarization is observed in all the directions of the film edges (*SI Appendix*, *Supplementary Note 7*). The monolayer spin spiral surprisingly indicates tunable bistability with magnetic field, originated from the net magnetic moments due to nonmultiples of spin spirals within a finite-sized domain. This offers a distinct route to manipulate the spin-spiral state from previous studies, and expects to be generalized to other spin-spiral materials. This system opens up a platform for studying the fundamental physics in helimagnetism such as magnon excitations (47) and also for studying spin states of single polarons at 2D limit (33).

Materials and Methods

Molecular-Beam Epitaxy Growth. The graphene substrate was obtained by high-temperature pyrolysis of SiC(0001) substrate with cycles of vacuum flashing treatment, the details of which are provided in ref. 48. The 1T-NiI_2 films were grown on the SiC supported bilayer graphene by evaporating NiI_2 powders (purity, 99.99%) with molecular beam epitaxy. The substrate was kept at 373 ~ 423 K to deposit NiI_2.

STM Measurements. The measurements were performed in a custom-made Unisoku STM (1500) system (15) mainly at 2 K unless described exclusively. The spin-averaged STM data were measured with an electrochemically etched W tip. The SPSTM data were taken with Cr-coated or Fe-coated W tips. All the W tip were flashed to ~2,000 K to remove oxides. While the Cr tip was prepared by coating ~10 layers of Cr (purity: 99.995%) on a flashed W tip, the Fe tip was prepared by coating ~30 layers of Fe on a flashed W tip, subsequently annealing at ~500 K for 3 min. The tunneling spectra were obtained through a lock-in detection of the tunneling current with a modulation voltage of 983 Hz. The conventional W tips and spin-polarized tips had been characterized on standard samples of Ag(111), antiferromagnetic monolayer $CrTe_2$, and Fe_4Se_5 films (15, 37), respectively, prior to the measurements. The topographic images and STS were processed by WSxM and Igor.

DFT Calculations. The calculations were performed using the generalized gradient approximation for exchange-correlation potential, the projected augmented wave method (49, 50), and a plane-wave basis set as implemented in the Vienna ab initio simulation package (51, 52). A kinetic energy cutoff of 700 (650) eV for the plane waves was used for structural optimization (calculations on the relative energies). Each spin-spiral order was modeled using a 10 × 10 q mesh within the first Brillouin zone of the unit cell using the generalized Bloch theorem (gBT) (53). Among them, we selected 29 noncollinear magnetic configurations exhibiting lower energies in the gBT calculations. They, together with six collinear magnetic configurations, were further considered using the supercell method (26), in which spin–orbit coupling (SOC) was included. The inclusion of SOC is crucial for comparing total energies and thus for finding the magnetic ground state. The spin-exchange coupling parameters were extracted on a Hamiltonian of $H = -\frac{1}{2}\left[\sum_{i,j} J_{ij} S_i \cdot S_j + \sum_{i,j} J_{ij}^{\perp} S_i \cdot S_j + \sum_{i,j} (K_{ij}^{\gamma} S_i^{\gamma} S_j^{\gamma}) + \sum_{i,j} B(S_i \cdot S_j)^2 + 2 \sum_i A_z S_z^2\right]$, where A_z represents the single-ion anisotropy, J_{ij} and $J_{ij}^{\perp}$ are the intra- and interlayer isotropic Heisenberg exchange parameters, B and K_{ij}^{γ} are the biquadratic and collinear Kitaev interaction parameters (26). The noncollinear magnetism is not primary related to the DMI, but the J_1-J_3 model, as discussed in refs. 26 and 27. The SOC effect is significant in monolayer NiI_2 due to the presence of the heavy iodine atoms. Accounting for SOC is crucial as it substantially influences the relative total energies of different magnetic configurations, thereby affecting their relative stabilities (26). Therefore, the SOC effect must be included to accurately determine the magnetic ground state of monolayer NiI_2. Moreover, SOC induces considerable Kitaev interactions, which is the primary reason causing magnetic moments rotating within the Ni-I plane. We constructed a parallelogram supercell with two vectors of $(6\boldsymbol{a}, 3\boldsymbol{b})$ and $(-3\boldsymbol{a}, 3\boldsymbol{b})$ [$(9\boldsymbol{a}, 11\boldsymbol{b})$ and $(-2\boldsymbol{a}, 1\boldsymbol{b})$] to model the spiral orders for monolayer (bilayer) NiI_2. We considered different rotational propagation periods, directions, and plane orientations. The shown ones in Fig. 5 *A* and *D* are the most energetically favored. There are two antiparallel propagation directions which are energetically degenerate. A vacuum layer over 20 Å along the z direction was adopted to eliminate interactions among image layers. The on-site Coulomb interaction was considered with a U value of 4.2 eV and a J value of 0.8 eV for Ni 3d orbitals, according to the literature (19, 54) and our test calculations (26). Grimme's semiempirical D3 scheme (55) for dispersion correction was employed in combination with the Perdew–Burke–Ernzerhof functional (PBE-D3). All atoms, lattice volumes, and shapes in each supercell were allowed to relax until the residual force on each atom was less than 0.01 eV/Å. The propagation vector $\boldsymbol{Q}$ can be defined as $\boldsymbol{Q} = \frac{1}{N_1} \cdot \boldsymbol{a}' + \frac{1}{N_2} \cdot \boldsymbol{b}'$. Here, N_1 and N_2 are numbers of Ni atoms in one spiral periodicity along the $\boldsymbol{a}$ and $\boldsymbol{b}$ directions in the real space, respectively, whereas $\boldsymbol{a}'$ and $\boldsymbol{b}'$ are the reciprocal lattice vectors of the NiI_2 unit cell (Fig. 5*A* and *SI Appendix*, Fig. S10). The magnetic moments complete a full 2π rotation along both the $\boldsymbol{a}$ and $\boldsymbol{b}$ directions over $9a_0$, implying $N_1 = N_2 = 9$. This gives our theoretical propagating vector of $\boldsymbol{Q}_{1L} = (1/9, 1/9, 0)$, i.e., (0.111, 0.111, 0). Similarly, our experimental propagating vector $\boldsymbol{Q}_{1L}$ is = (1/9.08, 1/9.08, 0), i.e., (0.110, 0.110, 0).

Note Added in Proof. After the completion of our manuscript, we were aware of a related study uploaded at similar time to arXiv by M. Amini et al. (arXiv: 2309.11217, which has got published in ref. 44). They also found the existence of a spin spiral, but the determined propagation vector is different from ours.

Data, Materials, and Software Availability. All raw data and simulation code will be deposited to the repository figshare (56). Additional data and plots are included in *SI Appendix*.

ACKNOWLEDGMENTS. We gratefully acknowledge the financial support from the National Key Research and Development Program of China (Grant Nos. 2022YFA1402400 and 2023YFA1406500), the National Natural Science Foundation of China (Grants Nos. 92265201, 92477137, 92477205, 12204534, 12174131, and 52461160327), the Ministry of Science and Technology of China (Grant No. 2018YFE0202700), the Strategic Priority Research Program of Chinese Academy of Sciences (Grant No. XDB30000000), the Fundamental Research Funds for the Central Universities, the Research Funds of Renmin University of China (Grant No. 22XNKJ30) (W.J.), and the China Postdoctoral Science Foundation (Grant No. 2022M713447) (N.L.). Calculations were performed at the Physics Lab of High-Performance Computing (PLHPC) and the Public Computing Cloud (PCC) of Renmin University of China.

Author affiliations: [a]School of Physics and Wuhan National High Magnetic Field Center, Huazhong University of Science and Technology, Wuhan 430074, China; [b]Beijing Key Laboratory of Optoelectronic Functional Materials and Micro-Nano Devices, School of Physics, Renmin University of China, Beijing 100872, China; [c]Key Laboratory of Quantum State Construction and Manipulation (Ministry of Education), Renmin University of China, Beijing 100872, China; [d]Chongqing Key Laboratory of Micro and Nano Structure Optoelectronics, School of Physical Science and Technology, Southwest University, Chongqing 400715, China; and [e]Department of Quantum Materials Research, Wuhan Institute of Quantum Technology, Wuhan 430206, China

1. Y. Tokura, S. Seki, Multiferroics with spiral spin orders. *Adv. Mater.* **22**, 1554 (2010).
2. X. Yao, Y. Wang, S. Dong, Noncollinear topological textures in two-dimensional van der Waals materials: From magnetic to polar systems. *Int. J. Mod. Phys. B* **35**, 2130004 (2021).
3. Y. Tokura, N. Kanazawa, Magnetic skyrmion materials. *Chem. Rev.* **121**, 2857–2897 (2021).
4. T. Kurumaji, Spiral spin structures and skyrmions in multiferroics. *Phys. Sci. Rev.* **5**, 20190016 (2020).
5. D. Bikaljević *et al.*, Noncollinear magnetic order in two-dimensional $NiBr_2$ films grown on Au(111). *ACS Nano* **15**, 14985–14995 (2021).
6. H. Xie *et al.*, Evidence of non-collinear spin texture in magnetic moiré superlattices. *Nat. Phys.* **19**, 1150–1155 (2023).
7. S. Wu *et al.*, Layer thickness crossover of type-II multiferroic magnetism in NiI_2. arXiv [Preprint] (2023). https://doi.org/10.48550/arXiv.2307.10686 (Accessed 20 July 2023).
8. K. Bergmann *et al.*, Interface-induced chiral domain walls, spin spirals and skyrmions revealed by spin-polarized scanning tunneling microscopy. *J. Phys. Condens. Matter* **26**, 394002 (2014).
9. W. Wulfhekel, C. L. Gao, Investigation of non-collinear spin states with scanning tunneling microscopy. *J. Phys. Condens. Matter* **22**, 084021 (2010).
10. D. Billerey *et al.*, Neutron diffraction study and specific heat of antiferromagnetic NiI_2. *Phys. Rev. A* **61**, 138–140 (1977).
11. T. Song *et al.*, Direct visualization of magnetic domains and moiré magnetism in twisted 2D magnets. *Science* **374**, 1140–1144 (2021).
12. Y. Wu *et al.*, A van der Waals interface hosting two groups of magnetic skyrmions. *Adv. Mater.* **34**, 2110583 (2022).
13. R. Wiesendanger, Spin mapping at the nanoscale and atomic scale. *Rev. Mod. Phys.* **81**, 1495 (2009).
14. W. Chen *et al.*, Direct observation of van der Waals stacking–Dependent interlayer magnetism. *Science* **366**, 983–987 (2019).
15. J. J. Xian *et al.*, Spin mapping of intralayer antiferromagnetism and field-induced spin reorientation in monolayer $CrTe_2$. *Nat. Commun.* **13**, 257 (2022).
16. M. Bode *et al.*, Chiral magnetic order at surfaces driven by inversion asymmetry. *Nature* **447**, 190–193 (2007).
17. S. Kuindersma, J. Sanchez, C. Haas, Magnetic and structural investigations on NiI_2 and CoI_2. *Physica B+C* **111**, 231–248 (1981).
18. D. Billerey *et al.*, Magnetic phase transition in anhydrous NiI_2. *Phys. Rev. A* **77**, 59–60 (1980).
19. A. S. Botana, M. R. Norman, Electronic structure and magnetism of transition metal dihalides: Bulk to monolayer. *Phys. Rev. Mater.* **3**, 044001 (2019).
20. M. Lu *et al.*, Mechanical, electronic, and magnetic properties of NiX_2 (X = Cl, Br, I) layers. *ACS Omega* **4**, 5714 (2019).
21. V. V. Kulish, W. Huang, Single-layer metal halides MX_2 (X = Cl, Br, I): Stability and tunable magnetism from first principles and Monte Carlo simulations. *Mater. Chem. C* **5**, 8734 (2017).
22. J. Y. Ni *et al.*, Giant biquadratic exchange in 2D magnets and its role in stabilizing ferromagnetism of $NiCl_2$ monolayers. *Phys. Rev. Lett.* **127**, 247204 (2021).
23. D. Amoroso, P. Barone, S. Picozzi, Spontaneous skyrmionic lattice from anisotropic symmetric exchange in a Ni-halide monolayer. *Nat. Commun.* **11**, 5784 (2020).
24. A. O. Fumega, J. L. Lado, Microscopic origin of multiferroic order in monolayer NiI_2. *2D Mater.* **9**, 025010 (2022).
25. X. S. Ni, D. X. Yao, K. Cao, In-plane strain tuning multiferroicity in monolayer van der Waals NiI_2. *J. Magn. Magn. Mater.* **613**, 172661 (2025).
26. N. S. Liu *et al.*, Competing multiferroic phases in NiI_2 mono- and few-layers. *Phys. Rev. B* **109**, 195422 (2024).
27. X. Li *et al.*, Realistic spin model for multiferroic NiI_2. *Phys. Rev. Lett.* **131**, 036701 (2023).
28. J. Sødequist, T. Olsen, Type II multiferroic order in two-dimensional transition metal halides from first principles spin-spiral calculations. *2D Mater.* **10**, 035016 (2023).
29. Q. Song *et al.*, Evidence for a single-layer van der Waals multiferroic. *Nature* **602**, 601 (2022).
30. H. Ju *et al.*, Possible persistence of multiferroic order down to bilayer limit of van der Waals material NiI_2. *Nano Lett.* **21**, 5126–5132 (2021).
31. Y. C. Jiang *et al.*, Dilemma in optical identification of single-layer multiferroics. *Nature* **619**, E40–E43 (2023).
32. R. W. G. Wyckoff, *Crystal Structures* (John Wiley, New York, 1963).
33. C. Franchini *et al.*, Polarons in materials. *Nat. Rev. Mater.* **6**, 560–586 (2021).
34. M. Cai *et al.*, Manipulating single excess electrons in monolayer transition metal dihalide. *Nat. Commun.* **14**, 3691 (2023).
35. N. M. Caffrey *et al.*, Changes in work function due to NO_2 adsorption on monolayer and bilayer epitaxial graphene on SiC(0001). *Phys. Rev. B.* **94**, 205411 (2016).
36. Y. Wang *et al.*, Switchable half-metallicity in A-type antiferromagnetic NiI_2 bilayer coupled with ferroelectric In_2Se_3. *NPJ Comput. Mater.* **8**, 218 (2022).
37. W. H. Zhang *et al.*, Spin-resolved imaging of antiferromagnetic order in Fe_4Se_5 ultrathin films on $SrTiO_3$. *Adv. Mater.* **35**, 2209931 (2023).
38. A. Kubetzka *et al.*, Spin-polarized scanning tunneling microscopy with antiferromagnetic probe tips. *Phys. Rev. Lett.* **88**, 057201 (2002).
39. W. H. Wang *et al.*, A centrosymmetric hexagonal magnet with superstable biskyrmion magnetic nanodomains in a wide temperature range of 100–340 K. *Adv. Mater.* **28**, 6887 (2016).
40. X. Z. Yu *et al.*, Real-space observation of a two-dimensional skyrmion crystal. *Nature* **65**, 901 (2010).
41. N. Romming *et al.*, Writing and deleting single magnetic skyrmions. *Science* **341**, 636–639 (2013).
42. T. Okubo, S. Chung, H. Kawamura, Multiple-q states and the skyrmion lattice of the triangular-lattice Heisenberg antiferromagnet under magnetic fields. *Phys. Rev. Lett.* **108**, 017206 (2012).
43. E. Rastelli *et al.*, Non-simple magnetic order for simple Hamiltonians. *Physica B+C* **97**, 1 (1979).
44. M. Amini *et al.*, Atomic-scale visualization of multiferroicity in monolayer NiI_2. *Adv. Mater.* **36**, 2311342 (2024).
45. Z. M. Zhang *et al.*, Atomic visualization and switching of ferroelectric order in β-In_2Se_3 films at the single layer limit. *Adv. Mater.* **34**, 2106951 (2022).
46. K. Chang *et al.*, Discovery of robust in-plane ferroelectricity in atomic-thick SnTe. *Science* **353**, 274 (2016).
47. S. H. Son *et al.*, Multiferroic-enabled magnetic-excitons in 2D quantum-entangled van der Waals antiferromagnet NiI_2. *Adv. Mater.* **34**, 2109144 (2022).
48. X. Yang *et al.*, Possible phason-polarons in purely one-dimensional charge order of Mo_6Se_6 nanowires. *Phys. Rev. X* **10**, 031061 (2020).
49. P. E. Blöchl, Projector augmented-wave method. *Phys. Rev. B* **50**, 17953 (1994).
50. G. Kresse, D. Joubert, From ultrasoft pseudopotentials to the projector augmented-wave method. *Phys. Rev. B* **59**, 1758 (1999).
51. G. Kresse, J. Furthmüller, Efficient iterative schemes for ab initio total-energy calculations using a plane-wave basis set. *Phys. Rev. B* **54**, 11169 (1996).
52. G. Kresse, J. Furthmüller, Efficiency of ab-initio total energy calculations for metals and semiconductors using a plane-wave basis set. *Comput. Mater. Sci.* **6**, 15 (1996).
53. L. M. Sandratskii, Noncollinear magnetism in itinerant-electron systems: Theory and applications. *Adv. Phys.* **47**, 91 (1998).
54. I. V. Solovyev, P. H. Dederichs, V. I. Anisimov, Corrected atomic limit in the local-density approximation and the electronic structure of d impurities in Rb. *Phys. Rev. B* **50**, 16861 (1994).
55. S. Grimme, Semiempirical GGA-type density functional constructed with a long-range dispersion correction. *Comput. Chem.* **27**, 1787 (2006).
56. M.-P. Miao *et al.*, Spin-resolved imaging of atomic-scale helimagnetism in mono- and bilayer NiI2. Figshare. https://doi.org/10.6084/m9.figshare.28238651. Deposited 4 September 2025.